

Fabrication of Nanosized Layered-MnO₂/Activated Carbon Composites Electrodes for High-performance Supercapacitor

Ya Liu¹, Songlin Zuo^{1,*}, Baoshou Shen², Yongfang Wang¹, Haiyan Xia¹

¹ College of Chemical Engineering, Jiangsu Provincial Key Lab for the Chemistry and Utilization of Agro-forest Biomass, Nanjing Forestry University, Nanjing 210037, China.

² Department of Environmental Engineering, College of Urban and Environmental Sciences Northwest University, Xi'an 710127, China.

*E-mail: zslnl@njfu.com.cn

Received: 11 April 2020 / Accepted: 8 June 2020 / Published: 10 July 2020

Layered-MnO₂/activated carbon composites were prepared by simply mixing activated carbons and Mn(NO₃)₂ solution, followed by heat treatment at 300 °C in order to develop high-performance and cost-effective active materials for supercapacitor electrodes. The effects of the loading mass of MnO₂, the surface chemistry and pore structure of activated carbons on the electrochemical performance of the composites as supercapacitor electrodes were investigated. The results show that layered α -MnO₂ nanoparticles of about 20 nm were synthesized in the activated carbons prepared by K₂S activation of lignin. A loading of 10 wt.% MnO₂ led to a two-fold increase in the specific capacitance of the activated carbon, reaching 294 F g⁻¹ at 5 mV s⁻¹ in 2 M KOH. The surface chemistry and pore structures of the supporters exert a significant effect on the electrochemical properties of the composites. Moreover, the as-prepared composites as supercapacitor electrodes possess excellent cycle stability and rate capability.

Keywords: activated carbons, layered-MnO₂, electrochemical properties, surface chemistry, pore structure

1. INTRODUCTION

Supercapacitors are a type of electric energy storage device and have attracted considerable attention due to their advantages, such as high power density and excellent cycle stability. Generally, electric double layer capacitance (EDLC) and pseudocapacitance are the two kinds of mechanisms to store electrical charges in supercapacitors. The former comes from the fast and reversible adsorption and desorption of electrolyte ions on the surface of active electrode materials in the process of electronically charging and discharging. Conversely, the electrical energy of the latter is mainly stored by transferring Faradaic charges between an electrolyte and electrode [1].

Carbon materials, including carbon nanotubes [2], graphene [3], carbon nanofibers [4], carbon nanocages [5], carbon microspheres [6] and activated carbon [7], are widely used as supercapacitor electrodes due to their good electrical conductivity and high surface area. They mainly contribute to EDLC and their actual capacitance is generally low at $\sim 200 \text{ F g}^{-1}$. As a result, supercapacitors using carbon materials as electrodes commonly have low energy density, which limits their large-scale applications. A significant number of metal oxides, such as RuO_2 [8], Co_3O_4 [9], TiO_2 [10], MoO_2 [11], NiO [12], IrO_2 [13,14] and MnO_2 [15], can trigger Faradaic electrical capacitance and thus significantly increase the energy density of supercapacitors. Therefore, metal oxide-loaded carbon materials are extensively studied to improve supercapacitor performance.

The precious metal oxide RuO_2 is a highly active substance that brings about a high pseudo-capacitance of above 1600 F g^{-1} [16]. The high cost and scarcity of RuO_2 , however, limit its commercial applications. In contrast, MnO_2 is low cost and highly available, and possesses a high theoretic capacity of 1370 F g^{-1} [17]. MnO_2 is therefore considered as a preferable alternative to RuO_2 as a supercapacitor electrode material. However, the poor electrical conductivity and low active area of MnO_2 hinder its application in energy storage devices [18]. Therefore, MnO_2 -like metal oxides are commonly loaded on electrically conductive carbon materials to prepare supercapacitor electrode materials with high performance. Novel carbon nanomaterials, such as carbon nanotubes [19], graphene [20], graphene oxide [21], carbon nanospheres [22] and carbon fibers [23], have been studied as supporters of MnO_2 . For example, Qian et al. fabricated a graphene- MnO_2 composite with a high specific capacitance of 800 F g^{-1} at a current density of 0.1 A g^{-1} [24].

Activated carbons are commercially available materials with highly developed pore structure and chemical stability, and thus have been widely used as supporters of metals and metal oxides. Moreover, the electrochemical properties of activated carbons can be tuned by regulating their pore structure and surface chemistry [7,25]. MnO_2 -loaded activated carbon composites have been reported as supercapacitor electrode materials [1,26,27], benefitting from the low cost of activated carbons compared with carbon nanomaterials. However, the investigations regarding MnO_2 -loaded activated carbon composites mainly focus on hybrid supercapacitor systems [15,27,28], and the reported specific capacitances of MnO_2 -loaded activated carbon composites are generally low at $100\text{--}300 \text{ F g}^{-1}$ [1,29,30], albeit it with high surface area activated carbons as the supporter of MnO_2 [15,29,31]. To the best of our knowledge, little information is available concerning the effect of the pore structure and surface chemistry of activated carbons on the electrochemical properties of MnO_2 /activated carbon composites.

Recently, we have been devoted to improving the electrochemical properties of activated carbons prepared from chemical and physical activation as electrodes for supercapacitors and fuel cells [7,32,33]. It is well known that the common approaches for preparing activated carbons include two types, physical activation and chemical activation. The former is to use gases such as steam, carbon dioxides or air as activation agents. The latter is to use chemicals such as ZnCl_2 , H_3PO_4 , KOH , NaOH , K_2CO_3 and Na_2CO_3 as activation agents. Herein, we prepared sulfur-containing activated carbons with a high surface area and highly developed mesoporsity by K_2S activation of lignin, an abundant biomass-derived residue. This activated carbon presents an excellent performance as the matrix for MnO_2 loading and thus favors synthesis of nanosized layered MnO_2 by simply impregnating activated carbon and a manganese nitrate solution with a subsequent heat treatment. As a result, nanosized layered MnO_2 /activated carbon

composites with an electrical capacitance of 294 F g^{-1} was obtained. Finally, the effect of the surface chemistry of activated carbons on the properties of the composite was addressed.

2. EXPERIMENTAL

2.1. Preparation of activated carbons

Two types of activated carbons with various pore structures and surface chemistry were prepared from the K_2S activation of lignin and steam activation of coconut shell-based chars. In the process of K_2S activation, 30 g of lignin was mixed with 250 mL of a certain concentration of potassium sulfide solution. The mixture was dried at $110 \text{ }^\circ\text{C}$ for 24 h and then heated in a muffle furnace to $800 \text{ }^\circ\text{C}$ at the rate of $3 \text{ }^\circ\text{C min}^{-1}$ for activation. The carbonized products were then taken out after cooling to room temperature and extensively washed with 0.1 M HCl and hot deionized water until the filtrate was pH 6–7. The sample was dried at $105 \text{ }^\circ\text{C}$ in an oven to constant weight. The obtained products are denoted as sulfur-containing activated carbon (LCX), where X represents the mass ratio of potassium sulfide to lignin ($X = 1$ or 2).

A steam activated carbon (CAC) was prepared from coconut shell (Linchang Charcoal Industry Company, Nanjing, China).

2.2. Surface chemical modification of activated carbon

Nitric acid oxidation. CAC was oxidized in 5 M HNO_3 at $80 \text{ }^\circ\text{C}$ for 4 h. The oxidized CAC was extensively washed with deionized water and then dried at $105 \text{ }^\circ\text{C}$ in an oven to constant weight. The obtained sample is denoted as CAC-O.

Ammonia modification. Ammonia modification of activated carbons was carried out in the vertical tube furnace. CAC-O was placed in an alundum crucible and heated at a rate of $5 \text{ }^\circ\text{C min}^{-1}$ under a N_2 gas flow. The gas flow was then switched from N_2 to NH_3 when the furnace temperature was elevated to $950 \text{ }^\circ\text{C}$. The activated carbon was kept at $950 \text{ }^\circ\text{C}$ in the NH_3 gas flow for 2 h. Finally, the sample was cooled to room temperature in the tube furnace under N_2 flow. The modified activated carbon materials are denoted as CAC-O-N.

Thiourea modification. In order to prepare sulfur-containing activated carbons, CAC was mixed with thiourea ($\text{CH}_4\text{N}_2\text{S}$) according to a CAC/ $\text{CH}_4\text{N}_2\text{S}$ mass ratio of 1:1 and then fully grinded for 20 min. The obtained mixture was heated in a vertical tube furnace to $180 \text{ }^\circ\text{C}$ for residence time of 1 h and then to $750 \text{ }^\circ\text{C}$ for residence time of 1 h at the rate of $10 \text{ }^\circ\text{C min}^{-1}$ under a N_2 (purity, 99.99%) atmosphere. After cooling to room temperature in a N_2 flow, the activated carbon was washed with 0.1 M HCl and hot deionized water until the pH of the filtrate was neutral. The modified CAC was dried at $105 \text{ }^\circ\text{C}$ in an air oven for 24 h and is denoted as CAC-S.

2.3. MnO₂ loading on activated carbon

For loading MnO₂ on activated carbon, 0.2 g of activated carbon was mixed with 50 mL of Mn(NO₃)₂ solution with various concentrations of 2.42, 3.63, 4.84, 7.26 and 9.68 mmol, and magnetically stirred at 25 °C for 24 h. After that, the mixture was dried in a freezing dryer for 48 h and then heated to 300 °C in an alundum crucible in a vertical tube furnace at a rate of 5 °C min⁻¹ under a N₂ gas flow for a residence time of 2 h. The obtained sample was labeled as X% MnO₂/activated carbon, where X indicates the mass of loaded MnO₂ that was obtained in terms of the activated carbon mass and the different concentration of Mn(NO₃)₂ with a given volume. These composites prepared with LC1, LC2, CAC, CAC-O, CAC-O-N and CAC-S as supporters are referred to as MnO₂/LC1, MnO₂/LC2, MnO₂/CAC, MnO₂/CAC-O, MnO₂/CAC-O-N and MnO₂/CAC-S.

2.4. Characterization of materials

The nitrogen adsorption isotherms of all samples were obtained by a Quantachrome Autosorb-iQ2 nitrogen adsorption instrument (Quantachrome, Florida, USA). Based on the nitrogen adsorption isotherms, the specific surface area (S_{BET}) of the materials was calculated by the Brunauer-Emmet-Teller (BET) equation. The total pore volume (V_{T}) of the sample was obtained in terms of the nitrogen adsorption capacity at a relative pressure of 0.99. The micropore volume (V_{mic}) of the sample was calculated from the Dubinin-Radushkevich equation, while the mesopore volume (V_{mes}) was obtained by subtracting V_{mic} from V_{T} . The pore size distribution was analyzed by the quenched solid density functional theory equation [7]. The elemental analysis was performed by an Elementar Vario EL Cube elemental analyzer (Elementar, Hanau, Germany). XRD patterns were obtained using a Rigaku Ultima IV X-ray diffractometer (Rigaku, Tokyo, Japan) with graphite monochromatized Cu K α irradiation ($\lambda = 0.154$ nm) at 5–80°. Fourier transform infrared (FTIR) spectra were recorded on a Bruker VERTEX 80 V infrared spectrometer (Bruker, Karlsruhe, Germany). XPS data were obtained with a Shimadzu AXIS Ultra DLD X-ray photoelectron spectrometer (Shimadzu, Kyoto, Japan) with monochromatized Al K α radiation. The curve fitting of the high-resolution spectra was conducted using a Shirley background and a mixed Gaussian-Lorentzian peak shape. High-resolution transmission electron microscopy (HRTEM) was performed with a JEOL JEM-2100 UHR electron microscope (JEOL, Tokyo, Japan) operated at 200 KV. The surface element distribution of the composite was studied by energy dispersive spectroscopy (EDS, Bruker, AXS, Quantax 400-30).

2.5. Electrochemical measurements

The electrochemical properties of the prepared electrodes were tested in a 2 M KOH electrolyte using a three-electrode system. Nickel foam (1×8 cm²) containing active material, acetylene black and polytetrafluoroethylene (8:1:1 wt.%) was used as the working electrode. The thin electrode film was dried in an oven at 110 °C for 12 h and then pressed on nickel foams under a pressure of 10 MPa. The as-prepared electrode sheet was placed in a vacuum drying oven at 110 °C for 4 h to constant weight. The platinum wire and Ag/AgCl were used as the counter and reference electrodes, respectively. Cyclic

voltammetry (CV), galvanostatic charge/discharge (GCD) and electrochemical impedance spectroscopy (EIS) were measured using a workstation (Zennium, Zaher Instrumentation, Germany). EIS was performed with a frequency range from 200 kHz to 0.01 Hz at an open circuit voltage.

According to the CV curve, the specific capacitance (C) was calculated according to Eq. (1) [34]:

$$C = \frac{1}{m \cdot \Delta V \cdot \nu} \cdot \int I(V) dV \quad (1)$$

where ΔV (V) is the potential window, $\int I(V) dV$ is the integral area of the discharge curve and ν ($V s^{-1}$) is the scan rate of the CV curves.

Based on the GCD curve, the mass specific capacitance was calculated according to Eq. (2) [35]:

$$C = \frac{2i \int V dt}{m \cdot V^2 \big|_{V_i}^{V_f}} \quad (2)$$

where i (A) is the discharge current, V_f (V) and V_i (V) are the end voltage and starting of the discharge voltage in a short period of time, respectively, $\int V dt$ is the integral area of the discharge curve and m (g) is the mass of active material.

3. RESULTS AND DISCUSSION

3.1. Physicochemical structure of $MnO_2/LC2s$

Figure 1 presents the nitrogen adsorption isotherms and pore size distribution of the $MnO_2/LC2s$ prepared with different loading dosages. Their surface area and pore volumes are listed in Table 1. It is clear that K_2S activation of lignin produced the activated carbon LC2 with a highly developed pore structure. The surface area and pore volume of LC2 reach $2490 m^2 g^{-1}$ and $1.981 cm^3 g^{-1}$, respectively. The initial part of the isotherm has significant uptake at low relative pressures, which evidences the presence of micropores. At intermediate and high relative pressures, the isotherm possesses a hysteresis loop, which corresponds to adsorption in mesopores [36]. The pores in LC2 are dominantly distributed in a size range from 2 to 8 nm (Fig. 1b).

Table 1. Pore structure parameters and specific capacitance of $MnO_2/LC2$ composites with different loadings.

Sample	$S_{BET}/m^2 g^{-1}$	$V_T/cm^3 g^{-1}$	$V_{mic}/cm^3 g^{-1}$	$V_{mes}/cm^3 g^{-1}$	^a Specific Capacitance/ $F g^{-1}$
LC2	2490	1.981	0.806	1.175	163
5% $MnO_2/LC2$	1973	1.371	0.631	0.740	247
7.5% $MnO_2/LC2$	1935	1.444	0.613	0.831	279
10% $MnO_2/LC2$	1884	1.299	0.618	0.681	294
15% $MnO_2/LC2$	1759	1.204	0.575	0.629	288
20% $MnO_2/LC2$	1510	1.147	0.485	0.662	279

^a Specific capacitance value obtained at a scan rate of $5 mV s^{-1}$.

The S_{BET} and pore volume of the $\text{MnO}_2/\text{LC2s}$ were obviously decreased with the increase in loading dosage of MnO_2 , with a more obvious decrease in V_{mes} than V_{mic} . The pore width of LC2 is reduced from the range of 0.5–10.0 nm to 0.5–4.5 nm (Fig. 1b). These results imply that MnO_2 was predominantly deposited in the mesopores of activated carbons. The $\text{MnO}_2/\text{activated carbon}$ composites still possess high surface area and pore volume even when 20% MnO_2 was deposited in the activated carbons. This developed pore structure facilitates electrolyte ions to diffuse into the pores, thus improving the electrochemical performance of the $\text{MnO}_2/\text{activated carbon}$ composites.

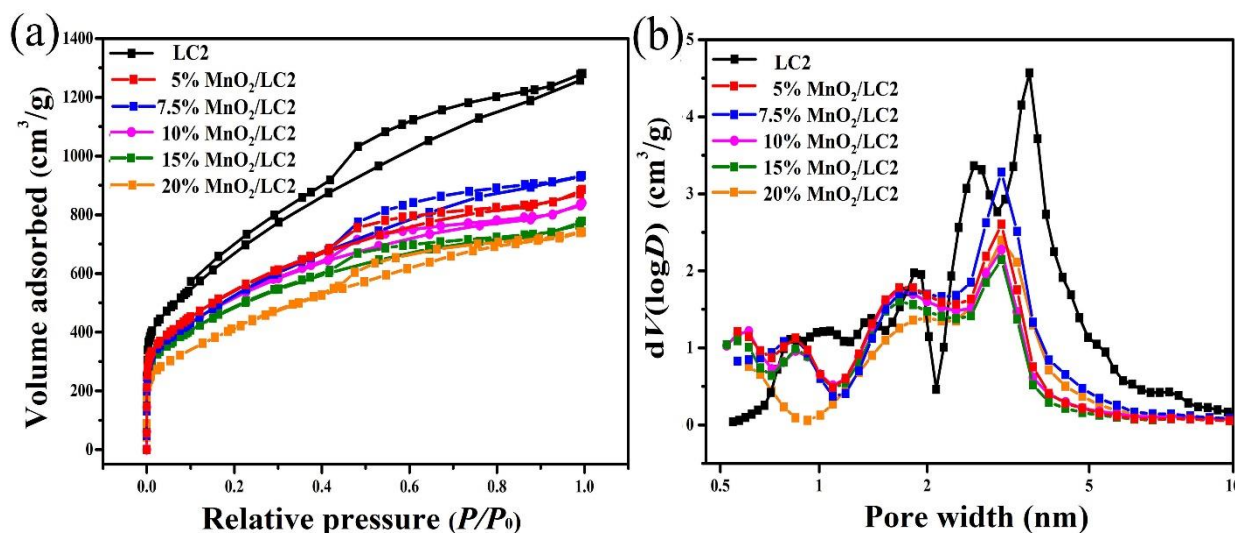


Figure 1. (a) Nitrogen adsorption-desorption isotherms and (b) pore width distributions of activated carbon and different loading of $\text{MnO}_2/\text{LC2}$ composites

Figures 2a and d show the HRTEM images of 10% $\text{MnO}_2/\text{LC2}$. It is clear that MnO_2 nanoparticles are deposited with a size of ~ 20 nm on the pores of activated carbons. Figure 2b shows the EDX spectra of LC2 and 10% $\text{MnO}_2/\text{LC2}$, which demonstrates that the as-prepared $\text{MnO}_2/\text{activated carbon}$ composites contain the C, S, Mn and O elements. EDS elemental analysis (Fig. 2b) shows that 10% MnO_2 -loaded activated carbon contains a Mn content of 5.5 wt.%, which is equivalent to 8.7 wt.% MnO_2 . This indicated that it is fairly easy to regulate the loaded- MnO_2 mass on activated carbons only by the mass ratio of activated carbons and $\text{Mn}(\text{NO}_3)_2$ in the solution in the preparation process employed here. The red area in the inserted photo of Fig. 2b is indicative of Mn atoms and thus revealed that MnO_2 was deposited in a particle on the carbon surface.

Figure 2c shows the XRD patterns of $\text{MnO}_2/\text{LC2s}$ prepared in different MnO_2 loading masses. It can be seen that all activated carbons exhibit a weak (002) peak at 23.6° and an obvious (100) peak at 43.4° . It is also noteworthy that MnO_2 loading resulted into a decrease in the intensity of the (100) peak of activated carbons, possibly caused by the partial oxidation of carbon. The $\text{MnO}_2/\text{activated carbon}$ composites show additional peaks at 36.89° , 48.33° , 54.50° and 65.80° , which are assigned to the diffraction peaks of the (211), (510), (601) and (002) planes of $\alpha\text{-MnO}_2$ crystal, respectively, according to the standard data file (JCPDS file no. 44-0141) [37]. Their intensities were enhanced by increasing MnO_2 loading dosages. Significantly, the HRTEM images (Figs. 2d and e) obviously showed that the

nanosized MnO_2 particles deposited on the surface of carbons possess a highly ordered layered structure, with interlayer distances of 0.48 and 0.36 nm. These interlayer distances are close to the different lattice spacings of $\alpha\text{-MnO}_2$ [38], which are consistent with the results of XRD analysis. The layered structures of $\alpha\text{-MnO}_2$ may promote efficient contacts between the active material and the electrolyte, which will provide more active sites for electrochemical reactions [39].

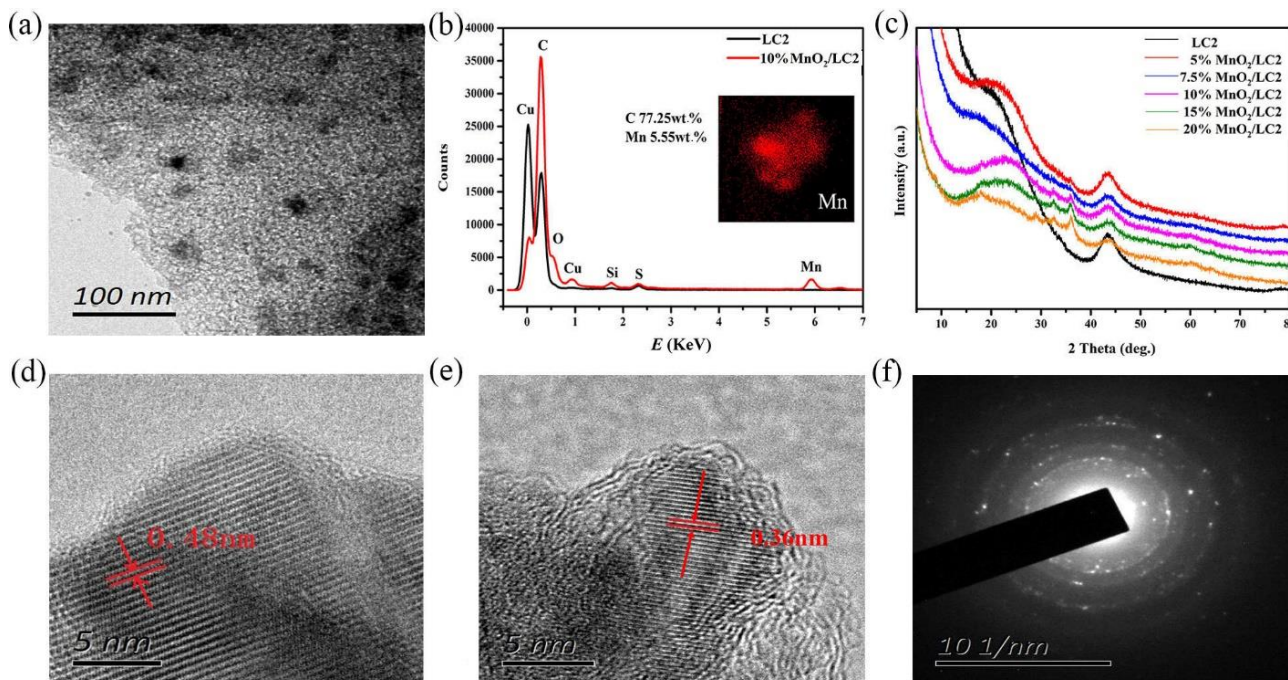


Figure 2. (a, d, e) HRTEM images of MnO_2 stripped from 10% $\text{MnO}_2/\text{LC2}$ at different magnifications; (b) EDX spectrum and EDS elemental map of 10% $\text{MnO}_2/\text{LC2}$ (insert); (c) XRD pattern of $\text{MnO}_2/\text{LC2}$ composite material with different loadings; (f) selected area electron diffraction pattern of 10% $\text{MnO}_2/\text{LC2}$

Figure 3a presents the FTIR spectra of 10% $\text{MnO}_2/\text{LC2}$ and LC2. They exhibit strong absorption bands at 3415, 2900, 1635, 1400 and 1300–1000 cm^{-1} . Among these, the bands at 3415, 2900, 1635 and 1300–1000 cm^{-1} are assigned to the stretching vibrations of O-H, C-H in methyl, C=C in aromatic ring and C-O, respectively [30]. The band at 1400 cm^{-1} is attributed to the bending vibration of C-H in methyl. The MnO_2 -loaded activated carbons exhibited additional strong peaks at 723, 645 and 532 cm^{-1} , which are attributed to the stretching Mn-O vibrations of MnO_2 . The results indicated that manganese oxides interacted with the surface functional groups of activated carbon and are then deposited on it. Figure 3b depicts the Mn 2p XPS spectrum of 10% $\text{MnO}_2/\text{LC2}$. Clearly, the Mn 2p XPS spectrum consists of two characteristic spin-orbit doublets, Mn 2p_{3/2} and Mn 2p_{1/2} centered at 641.8 and 653.4 eV, respectively, which is in excellent agreement with the Mn 2p XPS data reported previously in MnO_2 [40,41]. This reveals that the manganese of manganese oxide nanoparticles mainly exists in a positive tetravalent state. The high-resolution O 1s spectrum of 10% $\text{MnO}_2/\text{LC2}$ (Fig. 3c) can be deconvoluted into four

component peaks at 530.0, 531.4, 531.7 and 533.3 eV, which are assigned to the Mn-O-Mn, the Mn-OH, the C=O/C-O and O-H, respectively [17,42].

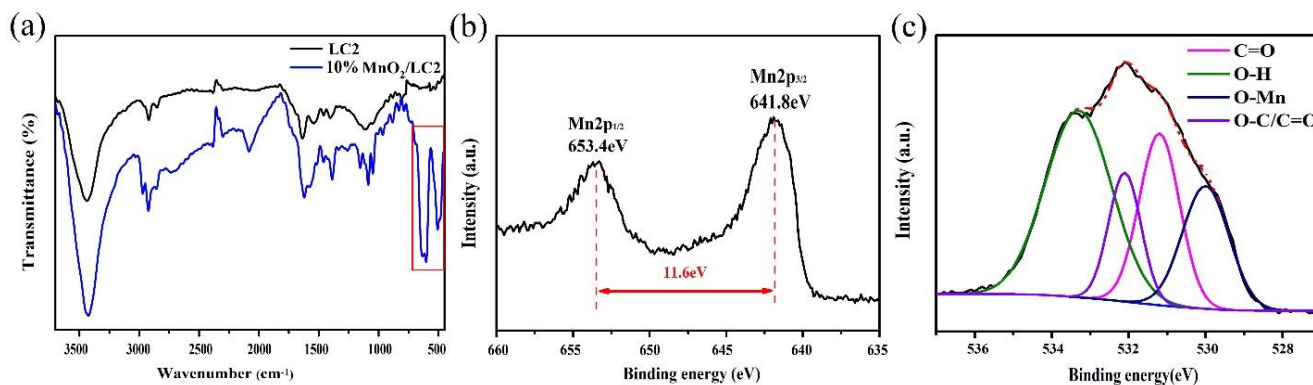


Figure 3. (a) FTIR spectra of LC2 and 10% MnO₂/LC2 composite material and high resolution XPS spectra of 10% MnO₂/LC2 composite: (b) Mn 2p and (c) O 1s

3.2. Electrochemical performance of MnO₂/LC2s

3.2.1. Electrochemical behavior

Figures 4a-c depict the CV curves of LC2 and MnO₂/LC2s at different scan rates in the three-electrode system in a 2 M KOH electrolyte. The CV curves of LC2 exhibit a common rectangular shape, indicating of a typical double-layer electric capacitance. The MnO₂/activated carbon composites, however, exhibit two redox peaks in the CV curves, suggesting that the redox reactions obviously happened in the composites and led to a remarkable Faradic capacitance. Moreover, the intensities of the redox peaks were lessened with the increase in the scan rate and nearly disappear up to 200 mV s⁻¹, indicating that the redox reaction was inhibited by the increased scan rate.

The charge/discharge curves of the activated carbons with different loading masses of MnO₂ at different current densities are shown in Figs. 4d-f. As can be seen, the GCD curves of the MnO₂/LC2s at 1 A g⁻¹ exhibit two distinct steps both in the charge and discharge curve sides at voltages of -0.45 and -0.55 V, which may imply that the redox reactions or battery behaviors happened obviously because of α -MnO₂ [37]. At 8 A g⁻¹, the GCD curves become symmetrical and the steps nearly disappeared. This discrepancy between 1 and 8 A g⁻¹ is consistent with the change in the CV curves by the varied scan rates.

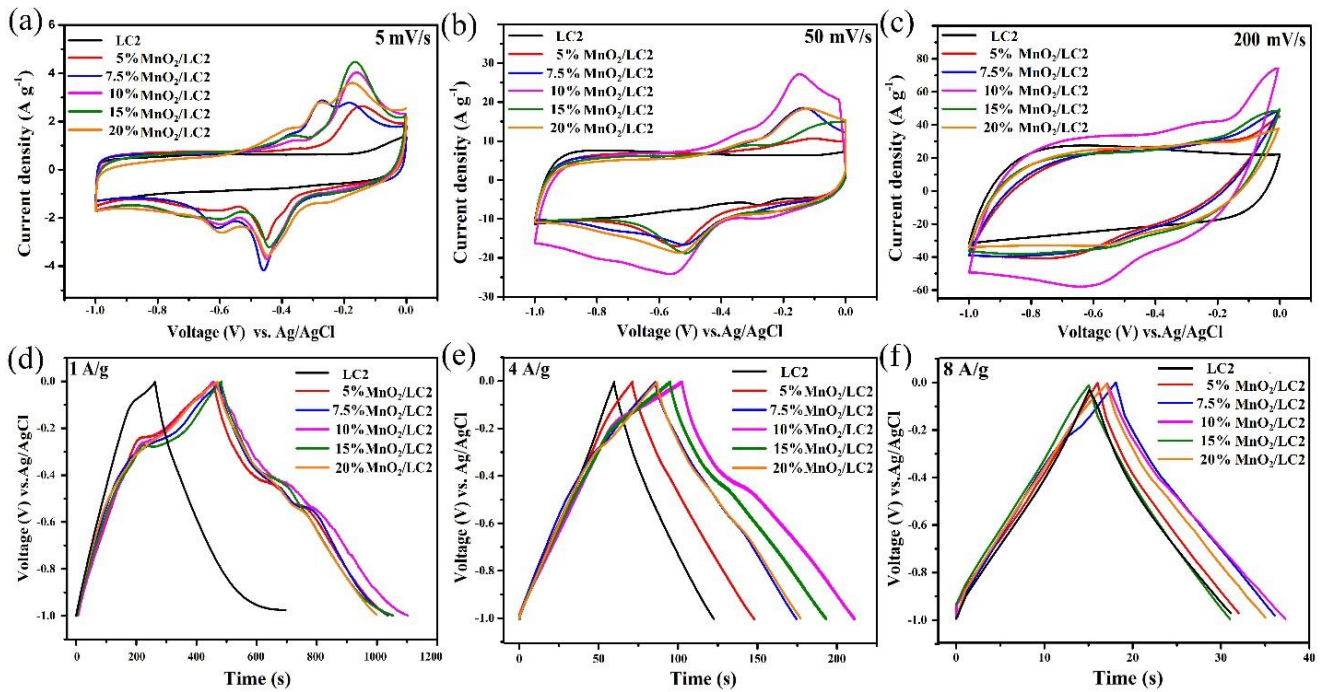


Figure 4. (a-c) CV curves at scan rates of 5, 50 and 200 mV s^{-1} ; (d-e) GCD curves at current densities of 1, 4 and 8 A g^{-1} of activated carbon with different mass loadings of MnO_2 in a 2 M KOH electrolyte

3.2.2. Specific capacitance

Table 2. Specific capacitance of MnO_2 -loaded carbon materials published in the literature (All values are measured using a three-electrode system)

Electrode material	Electrolyte	Current density or scan rate	Specific capacitance (F g^{-1})	Ref.
MnO_2/CNT	0.5 M Na_2SO_4	0.2 A g^{-1}	162	[19]
$\text{MnO}_2/\text{graphene}$	1 M Na_2SO_4	5 mV s^{-1}	292	[20]
MnO_2/CNF	1 M Na_2SO_4	2 mV s^{-1}	900	[23]
MnO_2/AC	1 M Na_2SO_4	1 A g^{-1}	221	[43]
MnO_2/AC	1 M Na_2SO_4	0.5 A g^{-1}	252	[44]
MnO_2/CNW	6 M KOH	1 A g^{-1}	465	[45]
MnO_2/MC	2 M KCl	5 mV s^{-1}	220	[46]
$\text{MnO}_2/\text{graphene}$	1 M Na_2SO_4	1 A g^{-1}	324	[47]
MnO_2/AC	1 M NaCl	5 mV s^{-1}	77.6	[48]
This work	2 M KOH	5 mV s^{-1}	294	
This work	2 M KOH	1 A g^{-1}	257	

CNF, AC, CNW and MC corresponded to carbon nanofiber, activated carbon, carbon nanowires and mesoporous carbon, respectively.

The specific electrical capacitance of activated carbons was calculated by the Eqs. (1) and (2) in terms of the CV and GCD curves, as listed in Fig. 5. Before loading with MnO₂, LC2 has a high electrical capacitance of 163 F g⁻¹ at 5 mV s⁻¹ and 139 F g⁻¹ at 1 A g⁻¹. The capacitance of LC2 is slightly decreased with the increase in the scan rates and the current density, indicating that LC2 has a high double electrical capacitance. MnO₂ loading resulted in a remarkable increase in the electrical capacitance, which reaches a maximum at a 10% loading dosage. The capacitance of 10% MnO₂/LC2 is as high as 294 F g⁻¹ in terms of the CV at a scan rate of 5 mV s⁻¹ and 257 F g⁻¹ from GCD at the current density of 1 A g⁻¹, which is almost double that of unloaded LC2. Table 2 lists the specific capacitance of MnO₂-loaded carbon materials reported previously. It can be seen that the as-prepared MnO₂/LC2 has a much higher capacitance than MnO₂-loaded activated carbons reported previously and, interestingly, even a higher value than MnO₂-loaded graphene, carbon nanotubes and carbon nanofibers. Therefore, we believe that activated carbons have a great potential in synthesizing with excellent electrochemical performance MnO₂/carbon material composites.

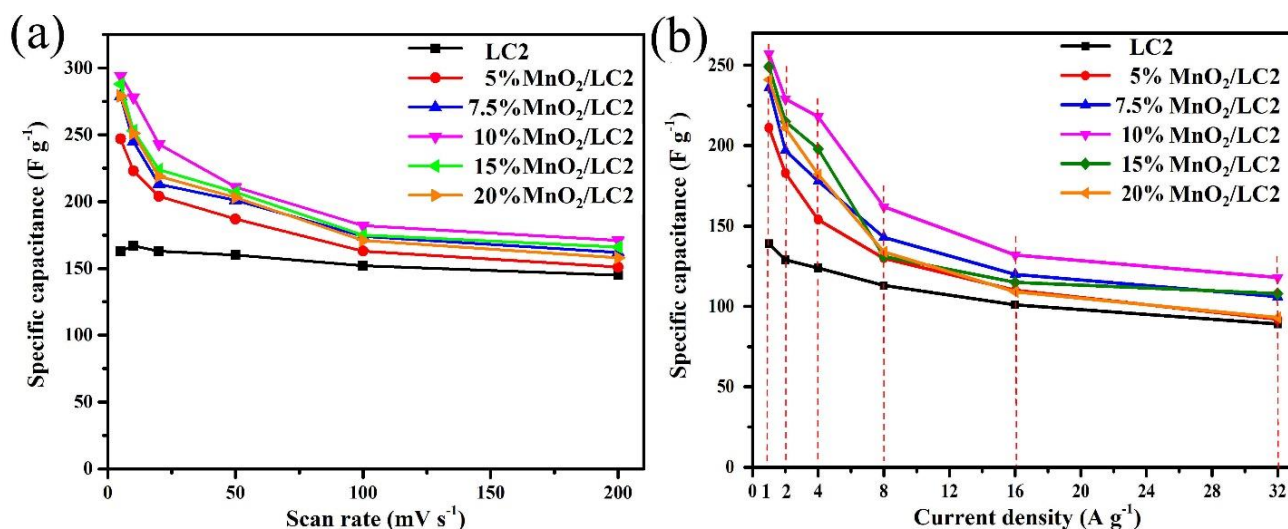


Figure 5. Specific capacitance of MnO₂-loaded activated carbons (a) at different scan rates from 5 to 200 mV s⁻¹ and (b) at different current densities from 1 to 32 A g⁻¹ in a 2 M KOH electrolyte

3.2.3. Electrochemical impedance and stability

As shown in Figure 6, all Nyquist spectra exhibit a semicircle diameter in the high frequency region, followed by a 45° Warburg impedance region in the intermediate frequency region, and a nearly vertical line in the low frequency. In the high frequency region, the intercept at the Z' real axis is the internal resistance (R_i) that consists of the electrolyte resistance, the intrinsic resistance of the electrode material and the contact resistance with a nickel foam current collector [34]. According to the parameters listed in Table 3, the R_i of all MnO₂/LC2s were less than that of LC2 (3.5 Ω). This is possibly because polar MnO₂ loaded in activated carbons leads to a decrease in the contact resistance between activated carbons and electrolyte ions, considering that MnO₂ is poor in electrical conductivity. Generally, in the

intermediate frequency region, the semicircle diameter of composites in the Nyquist spectra become larger with the increase in the MnO_2 loading dosage, indicating an increase in the charge transfer resistance (R_{ct}) at the interface between the active electrode material and the electrolyte [49], and the appearance of pseudocapacitance. In the low frequency region, the slopes of the Nyquist plot were determined by the diffusion resistance of the electrolyte ions to the electrode surface. All Nyquist plots displayed nearly vertical lines, which is caused by the activated carbon LC2 having a high surface area and a well-developed mesopore volume, to facilitate the electrolyte ions to diffuse into the inside of the electrode at a higher rate.

Table 3. Overall resistance R_i and R_{ct} measured in a 2 M KOH electrolyte

Sample	R_i/Ω	R_{ct}/Ω	Sample	R_i/Ω	R_{ct}/Ω
LC2	3.56	0.86	10% $\text{MnO}_2/\text{LC2}$	0.89	5.64
5% $\text{MnO}_2/\text{LC2}$	0.89	0.44	15% $\text{MnO}_2/\text{LC2}$	2.34	13.95
7.5% $\text{MnO}_2/\text{LC2}$	1.34	2.47	20% $\text{MnO}_2/\text{LC2}$	2.09	12.35

To evaluate the cycle stability of the 10% $\text{MnO}_2/\text{LC2}$ electrode, we used GCD to investigate the long-term charge/discharge behavior at a current density of 8 A g^{-1} , as shown in Fig. 6b. The specific capacitance was retained up to 83.6% after 5000 cycles, which is better than those of the previously reported MnO_2 -loaded carbon materials [50–52]. This result indicates that the as-prepared layered- MnO_2 /activated carbon composites possess excellent cycle stability.

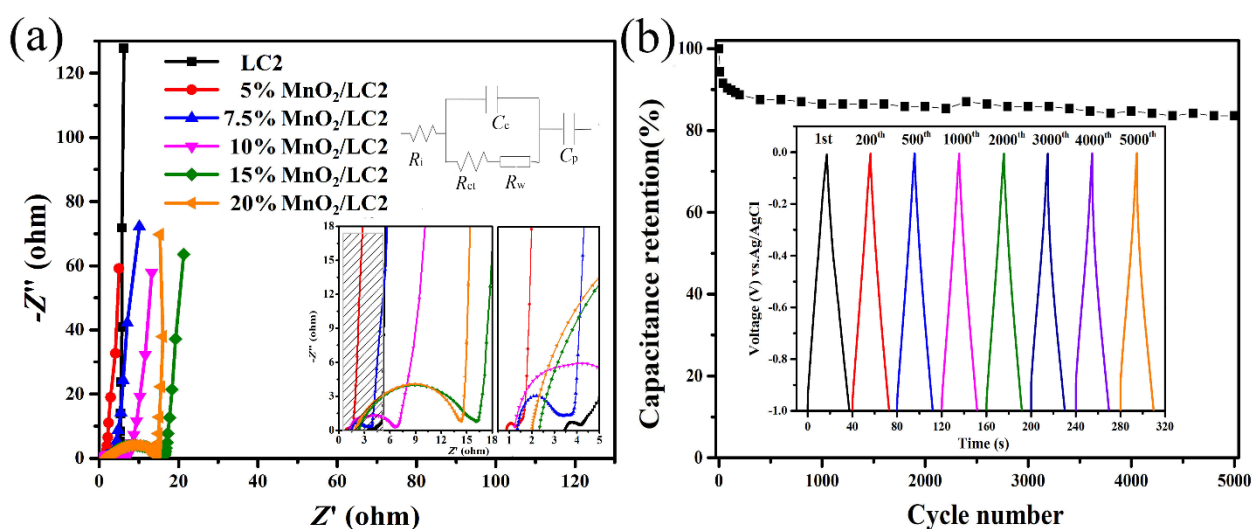


Figure 6. (a) Nyquist plots with insets showing the high-frequency parts and equivalent circuit of activated carbon with different mass loadings of MnO_2 (b) Cycle stability and GCD curves (inset) at different cycle numbers of 10% $\text{MnO}_2/\text{LC2}$ composite electrode at 8 A g^{-1} tested in a 2 M KOH electrolyte

3.2.4. Contribution of loaded MnO₂ to capacitance

In order to elucidate the contribution of loaded MnO₂ to the specific capacitance $C(\text{MnO}_2)$ of the MnO₂/activated carbon composite, $C(\text{MnO}_2)$ was obtained according to Eq. (3) in terms of CV curves at different scan rates and GCD curves at different current densities, as listed in Table 4.

$$C(\text{MnO}_2) = \frac{C(T) - C(\text{LC2})}{\text{the percentage of mass loading of MnO}_2} \quad (3)$$

where $C(T)$ and $C(\text{LC2})$ are the capacitance of the MnO₂/activated carbon composite and activated carbon, respectively.

Table 4. Contribution capacitance of supported MnO₂

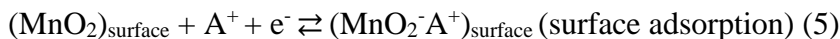
Sample	$C(\text{MnO}_2)/ \text{F g}^{-1}$											
	Scan rate / mV s^{-1}						Current density / A g^{-1}					
	5	10	20	50	100	200	1	2	4	8	16	32
5% MnO ₂ /LC2	1680	1120	820	540	220	120	1440	1080	600	340	180	60
7.5% MnO ₂ /LC2	1546	1040	667	547	293	226	1293	906	720	400	253	227
10% MnO ₂ /LC2	1270	1110	800	510	300	260	1180	950	910	490	310	290
15% MnO ₂ /LC2	833	573	406	313	153	140	733	573	493	120	93	140
20% MnO ₂ /LC2	580	420	280	215	95	65	510	410	290	105	40	20

Noticeably, the specific capacitance of loaded MnO₂ in 5% MnO₂/LC2 is higher than the pseudocapacitance theoretical value of 1370 F g⁻¹ [17] and those of 7.5% MnO₂/LC2 and 10% MnO₂/LC2 are similar to the theoretical value. Such high specific capacitance of loaded MnO₂ could be attributed to the following components: (i) typical battery behavior caused by redox reactions that take place in MnO₂ nanoparticles. This is confirmed by Fig. 4 where the CV curves exhibit two redox peaks and the GCD curves with two relatively small plateau at relatively small current density [26]. This also can be supported by the cycling stability of the composite, as shown in Fig. 6b and Fig. S2, where the capacity retention at 2 A g⁻¹ (76.4% after 1200 cycles) decreases faster than that at 8 A g⁻¹ (83.6% after 5000 cycles), which is characteristic of battery behavior; (ii) pseudocapacitance due to the Faradaic redox reaction of MnO₂; (iii) the EDLC of MnO₂ nanoparticles because of their contribution to the surface area. The pseudocapacitance and EDLC contribution can be expressed according to Eq. (4) [53]. Of course, MnO₂ loading led to a decrease in surface areas of activated carbons to some degree and thus an inevitable decrease in the EDLC of activated carbons. Therefore, the contributed capacitance of loaded MnO₂ at lower scan rates or less current densities mainly comes from the battery reactions and pseudocapacitance.

$$C_{\text{SP}} = \frac{nF}{M\Delta E} + C_d A_{\text{SP}} \quad (4)$$

where F is the Faraday constant, n the number of electrons transferred between the reduced and oxidized sites of the adsorbed species, M is the relative molecular mass, ΔE is the potential window, C_d

is the double layer capacitance and A_{SP} is the specific area of the material in contact with the electrolyte used.



With the increase in the scan rate to 50 mV s^{-1} and the current density to 8 A g^{-1} , the battery behavior almost vanished (Fig. 4) and therefore the pseudocapacitance based on the Faradaic redox reactions at the interface of the active material and the electrolyte is the main contribution to the capacitance of the electrode. The contributed capacitance of the loaded MnO_2 in 10% $\text{MnO}_2/\text{LC2}$ was decreased to 510 F g^{-1} at 50 mV s^{-1} and 490 F g^{-1} at 8 A g^{-1} , which is $\sim 36\%$ of the theoretical pseudocapacitance value of 1370 F g^{-1} and higher than the previously reported capacitance of MnO_2 that was deposited in sponge or multiwall carbon nanotubes [54,55]. Obviously, the results indicate that the MnO_2 composites exhibits a high rate capability and the high capacitance of the composite is essentially caused by the highly ordered layered $\alpha\text{-MnO}_2$. Generally, the pseudocapacitance of MnO_2 comes from the Faradaic redox reactions that take place on the surface of MnO_2 nanoparticles by the surface adsorption mechanism of electrolyte ions and inside bulk MnO_2 nanoparticles with the intercalation-extraction mechanism of electrolyte ions (A^+), such as K^+ and Na^+ , as shown in Eqs. (5) and (6) [56]. It is easily understood that an increase in the scan rate or current density impede the intercalation of electrolyte ions into bulk MnO_2 , thus leading to a reduction in the utilization efficiency of MnO_2 active materials and eventually a decrease in the pseudocapacitance of loaded MnO_2 . In addition, it can explain the fact that the capacitance of loaded MnO_2 (Table 4) was decreased with the increase in loading mass of MnO_2 in activated carbons.

3.3. Effect of activated carbon supporters

We prepared a series of activated carbons by different activation and modification methods in order to elucidate the effect of pore structure and surface chemistry of activated carbon supporters on the electrochemical performance of MnO_2 -loaded activated carbons. Table 5 and S1 list the information on the pore parameters, element contents and the electrical capacitance of all supporters before and after loading with MnO_2 . The element analysis (Table S1) and XPS spectra (Fig. S3 in the Supplementary information) showed that the surface chemistry of CAC-O is characteristic of oxygen-containing groups, including carboxyl, phenolic hydroxyl and carbonyl, CAC-S is sulfur-containing, including sulfone and thiophene groups, and CAC-O-N is nitrogen-containing groups, including pyridine, pyrrole and quaternary groups.

Figures 7a and b show the CV curves at a scan rate of 5 mV s^{-1} and the GCD curves at a current density of 1 A g^{-1} of all MnO_2 -loaded activated carbons after loading of MnO_2 in a three-electrode system in 2 M KOH electrolyte, respectively. The specific capacitance was calculated by CV curves at 5 mV s^{-1} (Table 5). It can be seen from Table 5 that surface chemical modification led to a change in pore structure, surface chemistry and specific capacitance of activated carbons, which is consistent with the previous investigations [57–59]. After loading with MnO_2 , the specific capacitance of the activated carbons was remarkably increased to 194 F g^{-1} for CAC, 198 F g^{-1} for CAC-S, 204 F g^{-1} for CAC-O-N

and 243 F g⁻¹ for CAC-O. Notably, except 10% MnO₂/LC1 and 10% MnO₂/LC2, 10% MnO₂/CAC-O has the highest capacitance among the MnO₂-loaded samples, although its surface area and pore volumes are significantly lower than the other MnO₂-loaded activated carbons. This is possibly because nitric acid oxidation improved the hydrophilicity of activated carbons and thus benefit the dispersion of MnO₂ nanoparticles that were highly dispersed in the pores of activated carbons in the preparation process. However, the increased capacitance of CAC, CAC-S and CAC-O-N are approximate (Table S1), although CAC-O-N has a higher surface area and pore volume (Table S1). This is possibly because CAC, CAC-S and CAC-O-N all underwent a heat treatment process at a high temperature and thus have similar hydrophobic features. Therefore, the surface chemistry of the activated carbons exerts an effect on MnO₂ loading and thus on the electrochemical performance.

Table 5. Pore structure parameters, element contents and specific capacitance at a scan rate of 5 mV s⁻¹ of different modified activated carbons

Sample	$S_{\text{BET}}/$ m ² g ⁻¹	$V_{\text{T}}/$ cm ³ g ⁻¹	$V_{\text{mes}}/$ V_{T} (%)	Elemental composition (wt.%)				Specific capacitance/F g ⁻¹
				C	N	O	S	
LC1	1906	1.310	49.1	91.18	2.11	6.34	1.83	159
LC2	2490	1.981	59.3	93.16	2.01	7.17	2.55	167
10% MnO ₂ /CAC	1471	0.728	25.7	77.34	1.58	3.89	0.19	194
10% MnO ₂ /CAC-O	968	0.466	27.7	67.28	2.68	16.56	0.27	243
10% MnO ₂ /CAC-O-N	1392	0.851	49.6	64.70	3.49	7.26	0.26	204
10% MnO ₂ /CAC-S	1357	0.645	27.3	74.81	1.57	5.74	2.87	198
10% MnO ₂ /LC1	1398	0.853	52.4	70.98	1.93	12.89	2.13	276
10% MnO ₂ /LC2	1884	1.299	53.4	72.74	2.08	13.73	2.05	294

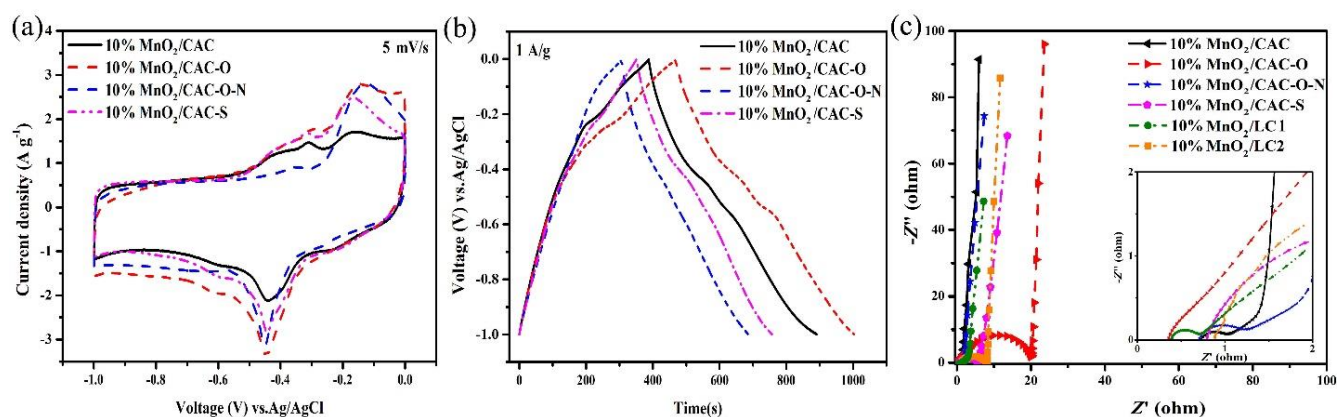


Figure 7. (a) CV curves at a scan rate of 5 mV s⁻¹, (b) GCD curves at a current density of 1 A g⁻¹ and (c) Nyquist plots of MnO₂-loaded activated carbon with different surface chemistry or pore structures in a 2 M KOH electrolyte

The supporters of CAC-O, LC1 and LC2 have higher oxygen contents (Table 5 and Table S1), indicating that they have similar hydrophilic surfaces. However, loading of 10% MnO₂ led to an increase in the specific capacitances of activated carbons by 109 F g⁻¹ for CAC-O, 117 F g⁻¹ for LC1 and 127 F

g^{-1} for LC2. This is attributed to the discrepancy between the pore structure of the supportors. Table 5 shows that LC2 had the best developed pore structures with the highest surface area and $V_{\text{mes}}/V_{\text{T}}$ value, while CAC-O was the lowest. The highly developed mesopore structure favors the loaded MnO_2 to be highly dispersed on the pores of supportors and thus improves the utilization efficiency of the electrochemically active materials. This is consistent with the previous findings that the developed pore structure provides a conductive network to enhance the charge transport to obtain a higher specific capacitance [60,61].

Figure 7c presents the Nyquist plots of these loaded- MnO_2 activated carbon electrodes from the different supportors. The internal resistance (R_i) of all samples is less than 1.0Ω , indicating that the as-prepared composite materials have good electrical conductivity. The charge transfer resistance (R_{ct}) of samples was increased with increasing oxygen contents of the composites (Table S1). Obviously, the 10% $\text{MnO}_2/\text{CAC-O}$ has the maximum semicircle diameter, with a R_{ct} of 19.5Ω .

4. CONCLUSIONS

In summary, the layered- MnO_2 /activated carbon composites were fabricated by mixing activated carbon and a $\text{Mn}(\text{NO}_3)_2$ solution, followed by heat treatment at $300 \text{ }^\circ\text{C}$. The highly ordered layered α - MnO_2 with a size of $\sim 20 \text{ nm}$ was deposited on the pores of activated carbons. Only through a loading of 10% MnO_2 , the specific capacitance of activated carbons could be remarkably increased two-fold, resulting in a high specific capacitance of 294 F g^{-1} at a scan rate of 5 mV s^{-1} in a 2 M KOH electrolyte. By comparing the electrochemical performance of the activated carbon with different activations and modifications, we found that the surface feature and pore structure of activated carbons exert a vital effect on the increased value in the capacitance of activated carbons after loading with MnO_2 . At a large current density of 8 A g^{-1} , the specific capacitance of the 10% $\text{MnO}_2/\text{LC2}$ reached 162 F g^{-1} and a total of 83.6% of the capacitance was retained after 5000 cycles in 2 M KOH , indicating the high rate capability and excellent cycle stability of the material. This suggests that such MnO_2 /activated carbon composites could be developed into electrode materials for high-performance supercapacitors.

ACKNOWLEDGEMENTS

This work was supported by the grant from National Key Research and Development Program Project Foundation (grant numbers 2017YFD0601006) and Jiangsu Natural science youth foundation (grant number BK20170928).

CONFLICT OF INTEREST

The authors declare no conflict of interest.

References

1. M. Kim, Y. Hwang, K. Min, J. Kim, *Electrochim. Acta*, 113 (2013) 322.
2. KH. An, WS. Kim, YS. Park, JM. Moon, DJ. Bae, SC. Lim, YS. Lee, YH. Lee, *Adv. Funct. Mater.*, 11 (2001) 387.

3. E. Senthilkumar, V. Sivasankar, BR. Kohakade, K. Thileepkumar, M. Ramya, GS. Sundari, S. Raghu, RA. Kalaivani, *Appl. Surf. Sci.*, 460 (2018) 17.
4. C. Ma, E. Cao, J. Li, Q. Fan, L. Wu, Y. Song, J. Shi, *Electrochim. Acta*, 292(2018) 364.
5. K. Xie, X. Qin, X. Wang, Y. Wang, H. Tao, Q. Wu, L. Yang, Z. Hu, *Adv. Mater.*, 24 (2012) 347.
6. C. Shao, S. Qiu, H. Chu, Y. Zou, C. Xiang, F. Xu, L. Sun, *Catal. Today*, 318 (2018) 150.
7. Y. Wang, S. Zuo, *Acta Physico-Chimica. Sinica*, 32 (2016) 481.
8. X. Wu, Y. Zeng, H. Gao, J. Su, J. Liu, Z. Zhu, *J. Mater. Chem. A.*, 1 (2013) 469.
9. SK. Meher, GR. Rao, *J. Phys. Chem. C.*, 115 (2011) 15646.
10. A. Ramadoss, SJ. Kim, *J. Alloys Compd.*, 561 (2013) 262.
11. M. Sarfraz, MFA. Aboud, I. Shakir, *J. Alloys Compd.*, 650 (2015) 123.
12. G. Zhang, L. Yu, HE. Hoster, XWD. Lou, *Nanoscale*, 5(2013) 877.
13. S. Korkmaz, FM. Tezel, İA. Kariper, *J. Alloys Compd.*, 754 (2018) 14.
14. A. Grupioni, E. Arashiro, T. Lassali, *Electrochim. Acta*, 48 (2002) 407.
15. T. Brousse, PL. Taberna, O. Crosnier, R. Dugas, P. Guillemet, Y. Scudeller, Y. Zhou, F. Favier, D. Bélanger, P. Simon, *J. Power Sources*, 173 (2007) 633.
16. C. Hu, K. Chang, M. Lin, Y. Wu, *Nano. Lett.*, 6 (2006) 2690.
17. M. Toupin, T. Brousse, D. Bélanger, *Chem. Mater.*, 16 (2004) 3184.
18. G. Yu, L. Hu, N. Liu, H. Wang, M. Vosgueritchian, Y. Yang, Y. Cui, Z. Bao, *Nano. Lett.*, 11 (2011) 4438.
19. H. Wang, C. Peng, F. Peng, H. Yu, J. Yang, *Mater. Sci. Eng. B.*, 176 (2011) 1073.
20. S. Qiu, R. Li, Z. Huang, Z. Huang, CP. Tsui, C. He, X. Han, Y. Yang, *Compos. Part. B-Eng.*, 161 (2019) 37.
21. S. Chen, J. Zhu, X. Wu, Q. Han, X. Wang, *ACS Nano.*, 4 (2010) 2822.
22. W. Du, X. Wang, J. Zhan, W. Du, X. Wang, J. Zhan, X. Sun, L. Kang, F. Jiang, X. Zhang, Q. Shao, M. Dong, H. Liu, V. Murugadoss, Z. Guo, *Electrochim. Acta*, 296 (2019) 907.
23. M. Zhi, A. Manivannan, F. Meng, N. Wu, *J. Power Sources*, 208 (2012) 345.
24. L. Qian, L. Lu, *Colloid. Surface A.*, 465 (2015) 32.
25. X. He, P. Ling, J. Qiu, M. Yu, X. Zhang, C. Yu, M. Zheng, *J. Power Sources*, 240 (2013) 109.
26. T. Yumak, D. Bragg, EM. Sabolsky, *Appl. Surf. Sci.*, 469 (2019) 983.
27. Y. Xue, Y. Chen, ML. Zhang, YD. Yan, *Mater. Lett.*, 62 (2008) 3884.
28. A. Bello, OO. Fashedemi, F. Barzegar, MJ. Madito, DY. Momodu, TM. Masikhwa, JK. Dangbegnon, N. Manyalaa, *J. Alloys Compd.*, 681 (2016) 293.
29. S. Wang, S. Jiang, X. Wang, *Electrochim. Acta*, 56 (2011) 3338.
30. A. Yuan, X. Wang, Y. Wang, J. Hu, *Energy Convers. Manage*, 51 (2010) 2588.
31. Y. Li, G. Wang, T. Wei, Z. Fan, P. Yan, *Nano. Energy*, 19 (2016) 165.
32. Y. Wang, S. Zuo, Y. Liu, *Electrochim. Acta.*, 263 (2018) 465.
33. Y. Wang, S. Zuo, M. Miao, Y. Liu, Z. Gu, *Int. J. Hydrogen Energy*, 44 (2019) 2811.
34. X. Zhao, Q. Zhang, C. Chen, B. Zhang, S. Reiche, A. Wang, T. Zhang, R. Schlögl, D. Su, *Nano. Energy*, 1 (2012) 624.
35. LQ. Mai, A. Minhas-Khan, X. Tian, KM. Hercule, YL. Zhao, X. Lin, X. Xu, *Nat. Commun.*, 4 (2013) 2923.
36. M. Thommes, K. Kaneko, AV. Neimark, *Pure Appl. Chem.*, 87 (2015) 1051.
37. H. Shen, Y. Zhang, X. Song, Y. Liu, H. Wang, H. Duan, X. Kong, *J. Alloys Compd.*, 770 (2019) 926.
38. B. He, G. Cheng, S. Zhao, X. Zeng, Y. Li, R. Yang, M. Sun, L. Yu, *J. Solid State Chem.*, 269 (2019) 305.
39. Q. Cheng, J. Tang, J. Ma, H. Zhang, N. Shinya, LC. Qin, *Carbon*, 49 (2011) 2917.
40. J. Mei, L. Zhang, *Electrochim. Acta*, 173 (2015) 338.
41. LH. Tseng, CH. Hsiao, DD. Nguyen, PY. Hsieh, CY. Lee, NH. Tai, *Electrochim. Acta*, 266 (2018) 284.

42. ZH. Huang, Y. Song, DY. Feng, Z. Sun, X. Sun, XX. Liu, *ACS Nano*, 12 (2018) 3557.
43. T. Huang, Z. Qiu, D. Wu, Z. Hu, *Int. J. Electrochem. Sci.*, 10 (2015) 6312.
44. X. Zhang, X. Sun, H. Zhang, D. Zhang, Y. Ma, *Mater. Chem. Phys.*, 137 (2012) 290.
45. B. Wang, J. Qiu, H. Feng, N. Wang, E. Sakai, T. Komiyama, *Electrochim. Acta*, 212 (2016) 710.
46. X. Dong, W. Shen, J. Gu, L. Xiong, Y. Zhu, H. Li, J. Shi, *J. Phys. Chem. B.*, 110 (2006) 6015.
47. Y. Qian, S. Lu, F. Gao, *J. Mater. Sci.*, 46 (2011) 3517.
48. YH. Liu, HC. Hsi, KC. Li, CH. Hou, *ACS Sustain Chem. Eng.*, 4 (2016) 4762.
49. W. Gu, M. Sevilla, A. Magasinski, AB. Fuertes, G. Yushin, *Energy Environ. Sci.*, 6 (2013) 2465.
50. C. Chen, W. Fu, C. Yu, *Mater. Lett.*, 82 (2012) 133.
51. J. Zhu, J. He, *ACS Appl. Mater. Interf.*, 4 (2012) 1770.
52. X. Feng, Z. Yan, N. Chen, Y. Zhang, Y. Ma, X. Liu, Q. Fan, L. Wang, W. Huang, *J. Mater. Chem. A.*, 1 (2013) 12818.
53. GZ. Chen, *Int. Mater. Rev.*, 62 (2017) 173.
54. W. Chen, RB. Rakhi, L. Hu, X. Xie, Y. Cui, HN. Alshareef, *Nano. Lett.*, 11 (2011) 5165.
55. SW. Lee, J. Kim, S. Chen, PT. Hammond, Shao-Horn Y., *ACS Nano*, 4 (2010) 3889.
56. B. Yin, S. Zhang, H. Jiang, F. Qu, X. Wu, *J. Mater. Chem. A.*, 3 (2015) 5722.
57. ND. Kim, W. Kim, JB. Joo, S. Oh, P. Kim, Y. Kim, J. Yi, *J. Power Sources*, 180 (2008) 671.
58. G. Xu, J. Han, B. Ding, P. Nie, J. Pan, H. Dou, H. Li, X. Zhang, *Green Chem.*, 17 (2015) 1668.
59. LZ. Fan, S. Qiao, W. Song, M. Wu, X. He, X. Qu, *Electrochim. Acta*, 105 (2013) 299.
60. Z. Fan, J. Yan, T. Wei, L. Zhi, G. Ning, T. Li, F. Wei, *Adv. Funct. Mater.*, 21 (2011) 2366.
61. D. Hulicova-Jurcakova, M. Seredych, GQ. Lu, TJ. Bandosz, *Adv. Funct. Mater.*, 19 (2009) 438.